

# Heterogeneous Pyrolysis: A Route for Epitaxial Growth of hBN Atomic Layers on Copper Using Separate Boron and Nitrogen Precursors

Gene Siegel,<sup>1,†</sup> Cristian V. Ciobanu,<sup>\*,‡,§,||</sup> Badri Narayanan,<sup>§</sup> Michael Snure,<sup>\*,†</sup> and Stefan C. Badea<sup>†</sup>

<sup>1</sup>KBRwyle, 2601 Mission Point Blvd., Dayton, Ohio 45431, United States

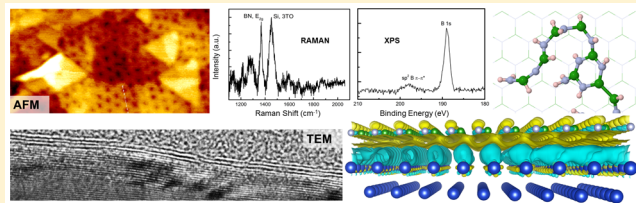
<sup>†</sup>Air Force Research Laboratory, Wright-Patterson AFB, Ohio 45433, United States

<sup>‡</sup>Department of Mechanical Engineering and Materials Science Program, Colorado School of Mines, Golden, Colorado 80401, United States

<sup>§</sup>Center for Nanoscale Materials, Argonne National Laboratory, Argonne, Illinois 60439, United States

## Supporting Information

**ABSTRACT:** Growth of hBN on metal substrates is often performed via chemical vapor deposition from a single precursor (e.g., borazine) and results in hBN monolayers limited by the substrates catalyzing effect. Departing from this paradigm, we demonstrate close control over the growth of mono-, bi-, and trilayers of hBN on copper using triethylborane and ammonia as independent sources of boron and nitrogen. Using density functional theory (DFT) calculations and reactive force field molecular dynamics, we show that the key factor enabling the growth beyond the first layer is the activation of ammonia through heterogeneous pyrolysis with boron-based radicals at the surface. The hBN layers grown are in registry with each other and assume a perfect or near perfect epitaxial relation with the substrate. From atomic force microscopy (AFM) characterization, we observe a moiré superstructure in the first hBN layer with an apparent height modulation and lateral periodicity of ~10 nm. While this is unexpected given that the moiré pattern of hBN/Cu(111) does not have a significant morphological corrugation, our DFT calculations reveal a spatially modulated interface dipole layer which determines the unusual AFM response. These findings have improved our understanding of the mechanisms involved in growth of hBN and may help generate new growth methods for applications in which control over the number of layers and their alignment is crucial (such as tunneling barriers, ultrathin capacitors, and graphene-based devices).



**KEYWORDS:** Multilayer boron nitride, heterogeneous pyrolysis, chemical vapor deposition, atomic force microscopy, moiré patterns

Hexagonal boron nitride (hBN) has emerged as an important two-dimensional (2D) insulator for applications ranging from inert substrates for graphene-based nanoelectronic devices,<sup>1,2</sup> to tunneling barriers<sup>3,4</sup> and atomically thin capacitors.<sup>5</sup> Progress in materials synthesis for these applications requires not only large area, high quality, and uniformity,<sup>6–10</sup> but also precise and reproducible control over the number of hBN layers and their orientation. With few exceptions,<sup>11,12</sup> hBN is largely grown from single precursors (borazine or ammonia borane),<sup>6,10,13–17</sup> which result in atomic monolayers on various metallic substrates. The morphology and alignment of these monolayers depends on the lattice mismatch and interactions between the  $\pi$  states of  $sp^2$  BN and the metal's d shell electrons. Atomically flat hBN monolayers can be grown on metals with filled or nearly filled d shells and small lattice mismatch like Cu (d<sup>10</sup>) and Pt (d<sup>9</sup>),<sup>18,19</sup> whereas on more strongly interacting metals with large mismatch (such as Ru) hBN forms a corrugated nanomesh.<sup>20,21</sup>

Significant progress has also been made recently in synthesizing multilayer hBN films with control over the number of layers, either one to a few<sup>11,22,23</sup> or more than ten

layers.<sup>11,24</sup> While procedures for controlling the layer thickness have been reported in these studies,<sup>9,11,22–24</sup> a key fundamental question remaining is the nature of the growth mechanism. In the case of growth from borazine on Fe or Fe alloy substrates,<sup>24,25</sup> the mechanism relies on catalytic cracking of the precursor and adsorption into the substrate, followed by precipitation to the surface and formation of hBN layers during cooling. There is clear evidence of this mechanism,<sup>24,25</sup> which is in fact akin to growth of graphene on catalytic metal surfaces whereby new layers grow under the old ones:<sup>26</sup> the number of layers depends on the solubility of boron and nitrogen (or carbon, in the case of graphene) into the metal surface and cooling temperature and rate. However, on Cu,<sup>23</sup> Ni,<sup>11</sup> or Pt<sup>22</sup> precipitation to the surface is not operational because the growth proceeds at a given temperature and longer exposure (rather than cooling below a certain point) leads to the

**Received:** December 30, 2016

**Revised:** March 6, 2017

**Published:** March 13, 2017

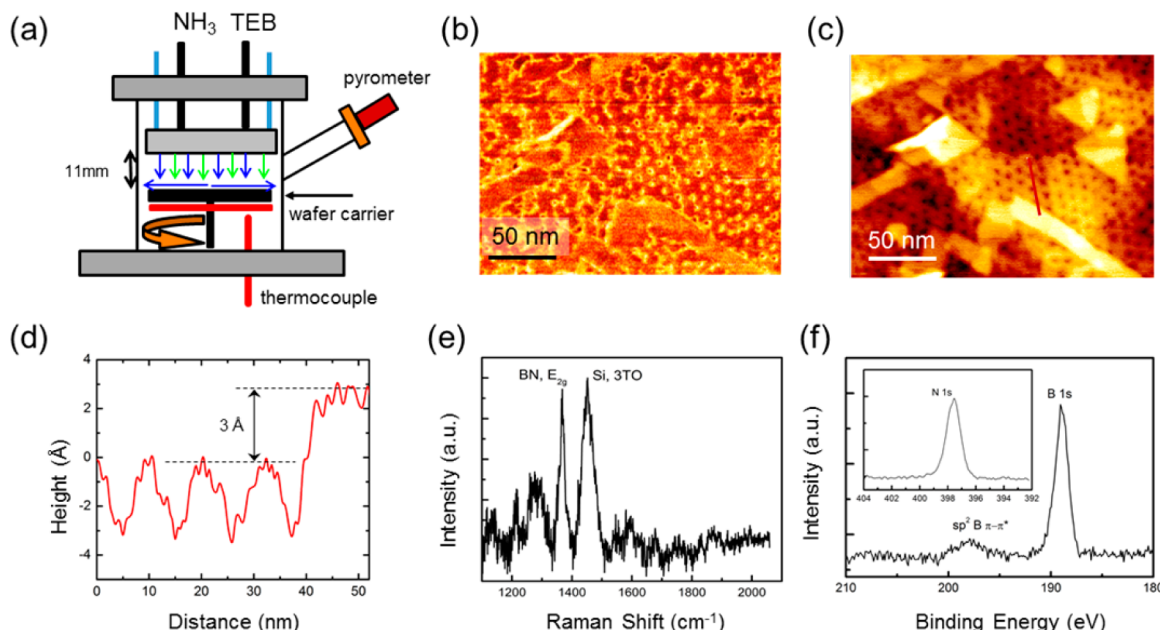


**Figure 1.** Mono- and bilayer hBN films grown on Cu(111). (a) Schematic of the low-pressure MOCVD reactor with actively cooled close coupled showerhead. (b,c) Typical AFM images showing (b) phase contrast and (c) height contrast. (d) Line profile illustrating the apparent height along the red segment in panel (c). (e) Raman spectrum of hBN after being transferred to a SiO<sub>2</sub>/Si substrate. (f) Chemical analysis of hBN films using XPS.

formation of new layers above the old ones, from one to a few and even tens of layers.<sup>11</sup> What makes the question of the mechanism truly puzzling is that the catalytic action of the substrate diminishes sharply after the deposition of one monolayer, as the substrate is passivated by hBN. This is consistent with many reports of surface-limited monolayer hBN growth from borazine.<sup>13–16</sup> A sort of catalytic transparency<sup>27</sup> of the metal substrate (through the first hBN layer) might be operational, but the catalytic action of the substrate effectively vanishes after one or two hBN layers passivate it. The issue of the mechanism leading to multilayer hBN growth was recognized and addressed by Ismach et al.,<sup>11</sup> who used diborane and ammonia as precursors; the authors ruled out surface-limited growth, precipitation from bulk (akin to graphene on Ni<sup>28</sup> or Pd<sup>29,30</sup>), and growth based on gas phase reactions, but have not conclusively settled on the mechanism responsible for the formation of multiple hBN layers. Alternatively, thick epitaxial hBN films can be grown by metal organic chemical vapor deposition (MOCVD) on inert substrates using high growth temperatures ( $\sim 1500$  °C).<sup>31–33</sup>

In this letter, we report on the growth of mono-, bi-, and trilayer hBN films on Cu(111), at lower temperatures than 1000 °C, from triethylborane (TEB) and ammonia as separate sources of B and N atoms. On the basis of density functional theory (DFT) calculations and characterization data, we suggest that the mechanism for growth of multiple layers is the activation of ammonia by boron and boron-containing radicals on the hBN covered surface. To ensure that these radicals are present on the surface regardless of whether it is already covered by hBN or not, we chose the substrate temperature to be sufficiently high (900 °C) so as to enable the pyrolysis of the TEB molecules on contact. This proposed mechanism, which we term heterogeneous pyrolysis, is markedly different than that leading to the formation of the first hBN layer, that is, surface adsorption followed by substrate-catalyzed dehydrogenation, polymerization of the

B–N radicals, and crystallization.<sup>24</sup> Although there are significant differences in the growth rates of the first layer and the subsequent ones, we find that the hBN layers are well aligned with each other, as well as with the Cu substrate. This is important for future devices in which such alignment is expected to lead to high-quality interfaces and low-dissipation electronic transport. Multiple characterization tools such as atomic force microscopy (AFM), transmission electron microscopy (TEM), Raman spectroscopy, and X-ray photo-electron spectroscopy (XPS) were employed to reveal the structure and morphology of the films. Our DFT calculations have shown that a modulated dipole layer forms at the interface between hBN and Cu, which interacts electrostatically with the AFM tip and leads to force modulations and hence to moiré patterns in height-contrast AFM images. Returning to the mechanism proposed for multilayer growth, we surmise that heterogeneous pyrolysis is not specific to copper but can operate on a wide range of substrates, even inactive ones such as sapphire.<sup>11,34</sup> Two conditions are necessary in order for heterogeneous pyrolysis to be expected to produce multilayer hBN films: (a) the precursors and the substrate temperature have to be chosen such that one of the precursors pyrolyzes and activates the other on the surface and (b) neither B or N atoms dissolve into the substrate during this pyrolysis and activation. While the first condition reduces to practical knowledge of precursors, the latter is satisfied if the metallic substrate is passivated with one hBN monolayer. Our findings can thus help generate new growth methods for applications in which control over the number of layers and their alignment is crucial (tunneling barriers, ultrathin capacitors, and graphene-based devices).

Using Cu(111) thin films on sapphire substrates, we have grown hBN samples by low-pressure MOCVD from TEB and NH<sub>3</sub> (Methods, and Supporting Information (SI), Figure S1). A cold wall MOCVD reactor with a close-coupled showerhead similar to that typically employed for conventional III-Nitride

MOCVD growth<sup>35</sup> was used (Figure 1a). For this reactor geometry, the TEB and NH<sub>3</sub> precursors are kept isolated at temperatures below their pyrolysis points, until their injection just above the heated substrate (900 °C). Under these conditions, TEB and NH<sub>3</sub> reach the surface with little interaction. Our precursor chemistry and reactor design are quite different from the majority of work reported on CVD growth of BN from a single B–N precursor in a hot wall reactor.<sup>6–9,11,22–24,36</sup> The use of separate B and N precursors allows us to explore a wide range of input N/B ratios. However, due to variations in thermal diffusion, adsorption/desorption rates, sticking coefficients, and precursor decomposition rates,<sup>37,38</sup> the actual concentration of active B and N species at the surface can be significantly different than the nominal (input) N/B ratio, which is in the range of 1000–1125 in our experiments. Because NH<sub>3</sub> has a pyrolysis temperature >900 °C,<sup>39</sup> it remains largely intact at the surface, which results in a significant drop in activated N/B ratio. As such, the availability and stability of adsorbed NH<sub>x</sub> ( $x = 1, 2, 3$ ) species on the surface is critical to the hBN growth process.

In the initial stages, hBN nucleates and grows quickly, covering the Cu surface in less than 2 min. After this initial period, second-layer islands nucleate sporadically and their coverage increases very slowly (Figure S2) with an average rate of  $\sim 3$  ML/h. In order to assess their quality, morphology, and composition, we have characterized the hBN films by a suite of techniques including AFM (Figure 1b–d), Raman (Figure 1e and Figure S3), and XPS (Figure 1f). Figure 1b,c displays typical phase contrast and height profile AFM images collected ex situ at room temperature in which the first hBN layer shows periodic superstructures while the second layer (bright areas in Figure 1c) does not. A line scan from the monolayer hBN region to the bilayer region (red segment in Figure 1c) shows an apparent height modulation for the monolayer regions; there is a height increase of 3–4 Å between the first and second hBN layers (Figure 1d and Figure S4), as well as between the second and third layer (Figure S5). This height increase is consistent with the known van der Waals (vdW) separation between hBN layers,<sup>40,41</sup> which we have also confirmed separately in TEM. After the layers were transferred onto SiO<sub>2</sub>/Si substrate, we performed Raman spectroscopy (Figure 1e and Figure S3). Figure 1e shows peaks at 1368 and 1450 cm<sup>-1</sup>, which correspond to the E<sub>2g</sub> vibrational mode of sp<sup>2</sup>-BN and the Si third TO mode, respectively.<sup>42</sup> The peak position and narrow width (fwhm of 20 cm<sup>-1</sup>) of the E<sub>2g</sub> Raman mode are indicative of the high quality of the films.<sup>43</sup> In addition, we also performed chemical analysis of the hBN films using XPS; this analysis has yielded a B/N ratio of 1/1.01, very close to perfect stoichiometry. The B 1s and N 1s photoelectron peaks were observed at 190.2 and 397.6 eV (Figure 1f, with inset), consistent with B–N bonding and in good agreement with previous reports for mono- to few-layer hBN.<sup>9</sup> At  $\sim 199$  eV, a small broad emission peak is also observed in Figure 1f, which is due to the  $\pi-\pi^*$  shakeup peak characteristic to sp<sup>2</sup> bonded BN.<sup>44</sup>

The morphology of our mono- and bilayer hBN films on Cu is illustrated in closer detail in Figure 2. Figure 2a shows the moiré patterns (superstructures) in phase-contrast AFM images for the single layer hBN regions. Similar to the height profile AFM images (Figure 1c), phase-contrast AFM images of bilayer hBN regions (Figure 2b) do not show any moiré patterns. While reports of moiré superstructures in phase-contrast AFM images are common,<sup>45</sup> there are two puzzling observations

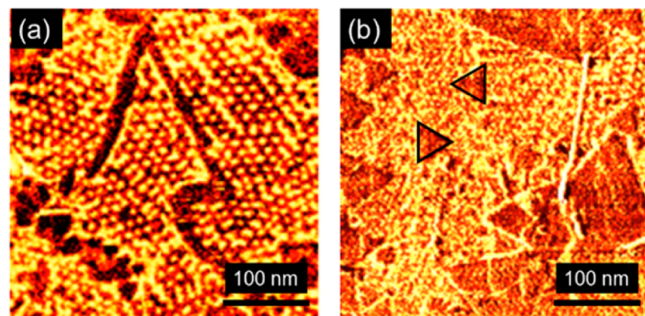


**Figure 2.** AFM images of hBN on Cu(111) for different growth times: (a) after 7 min, when only single layer hBN are present (moiré patterns), and (b) after 15 min, when second-layer hBN islands have nucleated and started to grow. To guide the eye, two of the triangular second-layer islands have been outlined with black borders.

emerging from our AFM characterization. The first observation is that height-contrast AFM images show moiré superstructures in an atomically flat first hBN layer. Second, the AFM images (both in phase- and height-contrast) of first and second hBN layers are drastically different; the second layer does not show any moiré patterns although it is in registry<sup>40,41</sup> with the first hBN layer that does exhibit periodic superstructures in AFM. We will discuss these findings next and explain them in terms of interfacial charge distributions.

The AFM observation of moiré patterns in height profile is highly unusual for the topographically flat, vdW-bonded hBN/Cu system. Electronic effects can accompany height variations in height-contrast AFM measurements, but are not normally detected by themselves. In order to explain this, we first note that variations of the forces detected by tapping mode AFM (which are eventually translated into height-contrast maps) can occur due to long-range electrostatic interactions between the AFM tip and the sample. We have used DFT calculations to understand how the electronic charge density is distributed<sup>46,47</sup> at the hBN–Cu interface as well as at the hBN–hBN/Cu interface with the former (latter) showing the electronic transfer to the first (second) hBN layer (Figure 3a,b). Figure 3a shows the interfacial electron transfer (defined in the Methods section) at the hBN–Cu interface with a gain of electronic density below the hBN layer and a density loss just above the Cu substrate. Despite in-plane inhomogeneities (Figure 3a), the charge transfer at the hBN–Cu interface effectively results in a dipole layer which interacts electrostatically with the (usually charged) AFM tip. The strength of the dipole layer is not constant, but rather modulated by the periodicity of the computational supercell, as shown in the top views of two cross sections through the interfacial charge distribution (Figure 3a, right). This in-plane modulation of the dipole strength leads to modulations in the average force between the charged AFM tip and the sample, hence explaining the moiré patterns observed in height-contrast AFM.

Given that the second hBN layer is in registry with the first,<sup>41</sup> one would expect the moiré periodicity to manifest itself through the second layer as well. As mentioned, our observations contradict this expectation. We have computed the charge transfer at the second interface with the results shown in Figure 3b. Interestingly, we find that electrostatic dipoles do not form a layer such as that between hBN and Cu(111) but have the staggered arrangement shown schematically by the up and down arrows in Figure 3b. The dipoles at the hBN–hBN/Cu interface change orientation from one site

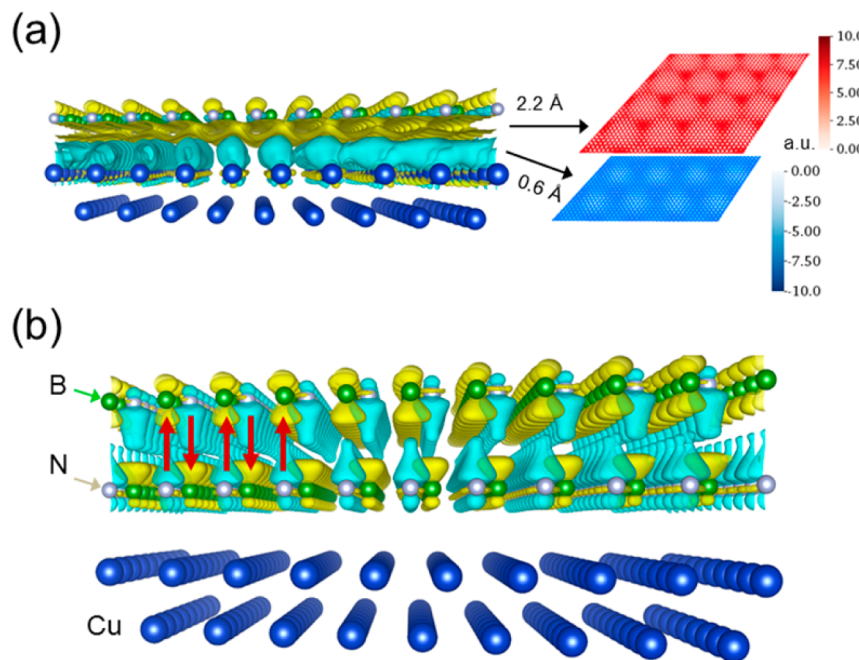


**Figure 3.** Electronic transfer plots for mono- and bilayer hBN on Cu. Positive (yellow) and negative (teal) isosurfaces at the interface between (a) the first hBN layer and Cu, and (b) between the first and second hBN layers. The isosurfaces shown are at  $\pm 0.00043 \text{ e/Bohr}^3$  and  $\pm 0.00011 \text{ e/Bohr}^3$  in (a) and (b), respectively. The right hand side of panel (a) displays planar views of the charge transfer for two planes situated at 0.6 and 2.2 Å above the top Cu layer, illustrating the formation of a modulated dipole layer at the hBN–Cu interface. Color scales densities of electronic gain (red) and loss (blue) are in arbitrary units.

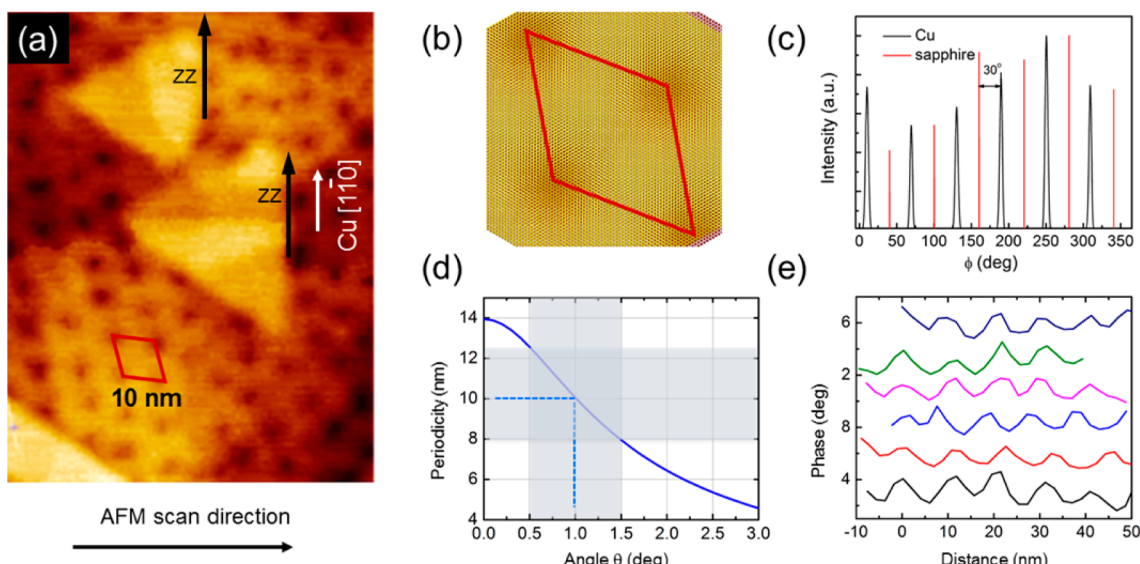


**Figure 4.** Epitaxial relationship for the hBN layers on Cu(111). (a) Height-contrast AFM images showing a close-up of the monolayer hBN moiré pattern and two second-layer islands. (b) Atomic structure of the 10 nm periodic moiré formed when the hBN zigzag (zz) direction is rotated by  $\theta = 1^\circ$  with respect to Cu[1̄10]. (c) X-ray  $\phi$ -scans of Cu on sapphire used for identifying the crystallographic directions in the Cu(111) film; these scans were taken after the growth of hBN/Cu/sapphire. (d) Spatial period of the moiré pattern as a function of the (misorientation) angle  $\theta$  between the hBN zigzag direction and Cu[1̄10]. Most misorientation angles observed fall between  $0.5^\circ$  and  $1.5^\circ$ , leading to patterns with periodicities between 8.0 and 12.5 nm. (e) Line profiles through phase-contrast AFM images showing spatial periodicities in the 8.0 to 12.5 Å range.

to another due to the registry of the two layers (AA' stacking), and therefore approximately cancel each other locally (Figure 3b). Because of this cancellation of neighboring dipoles (Figure 3b), the interface between the two hBN layers does not acquire a significant dipole moment per unit area. At the same time, the effect of the dipole from the first interface (hBN–Cu) is now diminished because the presence of the second hBN layer leads to a larger spacing between the AFM tip and the hBN–Cu

dipole layer. If we assume that there are induced dipoles on the AFM tip (which is made of doped silicon) and that the second hBN layer effectively doubles the distance between the tip and the hBN–Cu dipoles, then the force on the AFM tip decreases by a factor of  $2^2$ ; this is because the dipole–dipole interaction potential varies as  $1/r^3$ .<sup>48</sup>

Next, we turn to discussing the epitaxial relationship between the first hBN layer and the substrate. This revealed in Figure 4a

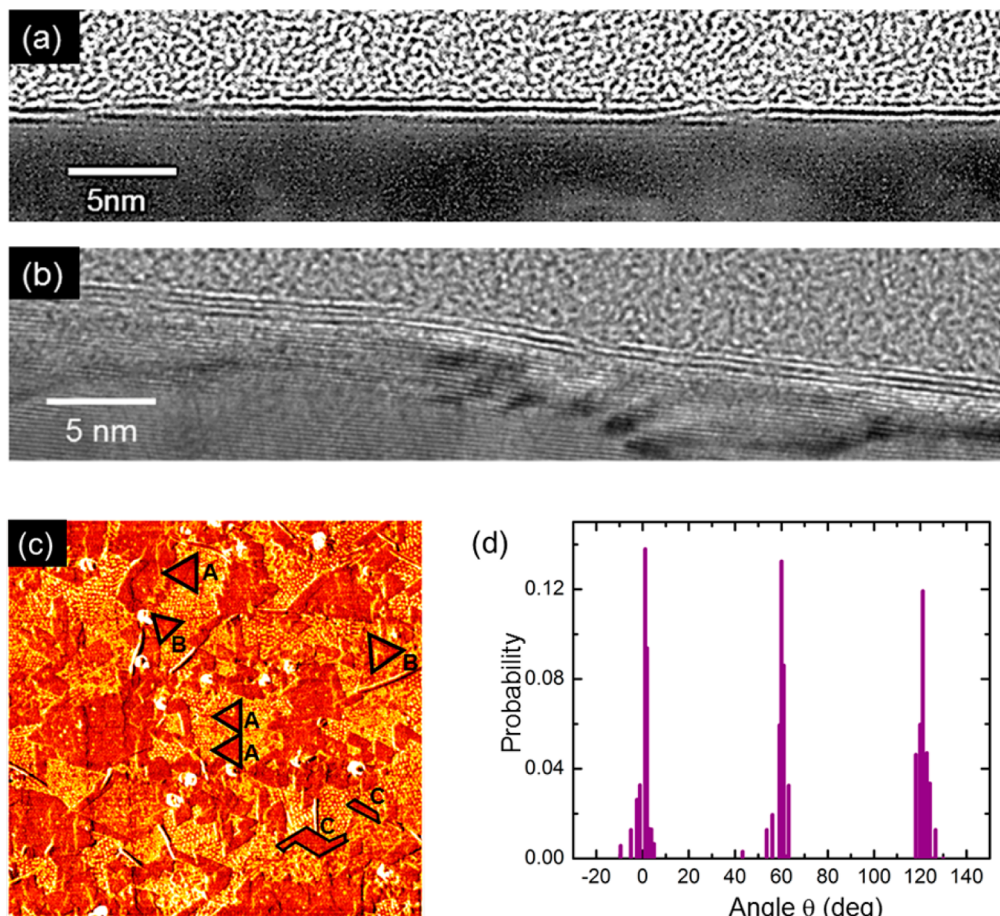


**Figure 5.** (a,b) TEM images of (a) two and (b) three layers of hBN on Cu(111). (c) Phase contrast AFM image ( $1 \mu\text{m} \times 1 \mu\text{m}$ ) showing different morphologies of the second-layer hBN islands, such as triangle-left (A), triangle-right (B), and ribbons (C). (d) Histogram of the orientations of all edges of the second layer islands in panel (c).

with supporting details in Figures 4b–e. This relationship was determined by performing X-ray  $\varphi$ -scans for Cu/sapphire and hBN/Cu/sapphire (Figure 4c) in combination with studying the lattice geometries of the hBN/Cu system (Figure 4b,d) and the spatial periodicities of AFM line scans (Figure 4e). First, we determined the axes of the Cu(111) substrate by performing X-ray  $\varphi$ -scans for Cu/sapphire. The  $\varphi$ -scans from the Cu(111) film and the sapphire (0001) substrate (shown in Figure 4c) reveal six symmetric diffraction peaks, indicating that the Cu is oriented with respect to sapphire such that  $\langle 111 \rangle \parallel \langle 0001 \rangle$  and  $\langle 110 \rangle \parallel \langle 11\bar{2}0 \rangle$ . With the sapphire [11\bar{2}0] direction identified, we aligned the AFM scan direction perpendicular to it (Figure 4a). In the scans acquired, we observed that one of the edges of triangular hBN islands was always nearly perpendicular to the AFM scan direction, and hence that edge was parallel with sapphire [11\bar{2}0] and with Cu[1\bar{1}0]. In a nitrogen-rich environment, the edges of triangular hBN islands (oriented at  $60^\circ$  with each other) are zigzag.<sup>49</sup> Thus, we established that the zigzag direction in the hBN layers is parallel (or nearly so) to Cu[1\bar{1}0] (Figure 4a).

To characterize the more precisely angular deviation  $\theta$  between a zigzag direction of hBN and the Cu[1\bar{1}0] axis, we have exploited our observation of moiré patterns in AFM in conjunction with lattice simulations of moiré superstructures. Such simulations are appropriate for vdW-bonded layers that do not change their lattice constants upon bonding, because the hBN–Cu bonding is weak<sup>18,46,50</sup> and yield spatial periodicities

that depend on the misorientation  $\theta$  and the values of the lattice constants. We have parametrized the lattice constants for BN and Cu so as to obtain the best agreement with previously published<sup>18</sup> moiré structure periodicities for hBN on Cu; this agreement was obtained for 2.511 and 2.560 Å for hBN and Cu, respectively. The values vary little from the experimental lattice constants of 2.50 Å for monolayer hBN,<sup>32</sup> and 2.556 Å for Cu(111) ( $= 3.615 \text{ \AA}/\sqrt{2}$ , because the room-temperature bulk lattice constant of Cu is 3.615 Å).<sup>51</sup> Consistent with other recent works,<sup>18</sup> we do not expect the uniform strain model to be able to cover subtleties of moiré structures (e.g., changes with temperature). The moiré periodicity varies rapidly with  $\theta$  (lattice simulation result, Figure 4d), going from 14 nm at  $0^\circ$  to 5 nm at  $3^\circ$ . The most prevalent spatial periodicity in our AFM images is  $\sim 10$  nm (atomic structure shown in Figure 4b), which is obtained for  $\theta = 1.0^\circ$  in the lattice simulations. Most moiré periodicities that we observed with AFM fall in the range from 8.0 to 12.5 nm (Figure 4e); based on the simulation results (Figure 4d), this implies that misorientation angles of the first hBN layer are all smaller than  $1.5^\circ$ . This alignment is consistent with a previous report of monolayer hBN island orientation on Cu<sup>32</sup> but shows significantly smaller misorientation angles.

With this assessment of the near-perfect alignment of the first hBN layer on Cu(111), we turn to discussing briefly the second and third layer. Figure 5a,b shows representative cross sectional TEM images of large-area, bi- and trilayer hBN films; these

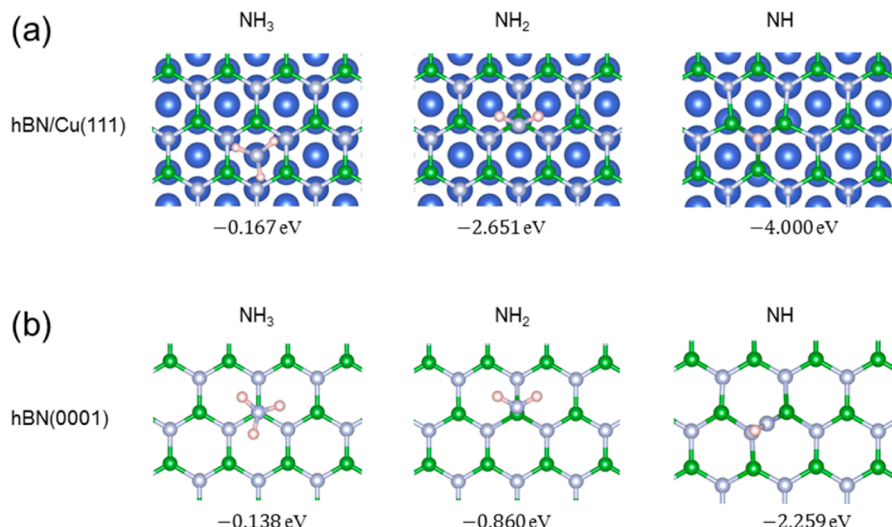


**Figure 6.** Top views of the most favorable adsorption positions for  $\text{NH}_3$  and its radicals on (a) hBN/Cu and (b) hBN(0001) with the latter used in order to efficiently model a fully passivated hBN/hBN/.../Cu substrate. The adsorption energies are given under each panel; they are negative to indicate that the adsorption is thermodynamically favorable, that is, exothermic.

images show straight, ordered hBN layers parallel to the (111) planes of the substrate. Taking a closer look at the orientation of the second layer islands, Figure 5c displays a large area AFM image in which these islands form shapes such as triangles pointing right, triangles pointing left, or ribbons (e.g., elongated parallelograms or trapezoids, Figure 5c). We have analyzed the orientation of each edge belonging to these islands, and plotted the results in the form of a histogram (Figure 5d). Figure 5d shows that within experimental uncertainties there are only three orientations for the edges of the second-layer islands, situated at  $60^\circ$  away from each other and parallel to the  $\langle 11\bar{2}0 \rangle$  (family of) directions in sapphire. This confirms that the second hBN layer is epitaxially aligned with the first, which is expected based on the most stable stacking in bulk hBN and also in bilayer hBN (AA').<sup>40,41</sup>

We now discuss a proposed mechanism for the growth on top an already present hBN layer, when the influence of the metal substrate on precursor reactions is negligible. Because the temperature of the substrate is significantly higher than the pyrolysis temperature of TEB, TEB adsorbs on the surface as boron atoms or boron-containing radicals. This indicates that the limiting steps for the growth of additional hBN layers are very likely the adsorption and dehydrogenation of ammonia and its radicals on the surface. Therefore, we discuss these steps prior to explaining the initial stages of growth of new layers on an hBN covered substrate. On bare Cu(111), adsorption and dehydrogenation of ammonia and its radicals are facilitated by the catalytic activity of the Cu substrate. The adsorption energies on bare Cu(111) are  $-0.819$  eV (for  $\text{NH}_3$  at the top site),  $-3.358$  eV ( $\text{NH}_2$ , bridge site), and  $-5.763$  eV ( $\text{NH}$ , fcc site); these are consistent with a previous report<sup>53</sup> that uses a different exchange-correlation energy functional. DFT calculations<sup>53</sup> show that the three dehydrogenation steps on bare Cu(111) encounter barriers of  $1.84$  eV ( $\text{NH}_3$  to  $\text{NH}_2$ ),  $1.59$  eV ( $\text{NH}_2$  to  $\text{NH}$ ), and  $2.19$  eV ( $\text{NH}$  to N). Although the temperature in our experiments  $900^\circ\text{C}$  ( $0.1$  eV) is significantly smaller than these activation energies on bare Cu, it still allows for the reactions to proceed when sufficient ammonia molecules are adsorbed. Indeed, we observed a relatively rapid formation of the first layer, consistent with previous reports<sup>6,43,44</sup> of hBN monolayers grown on Cu(111).

The catalytic influence of underlying Cu substrate is diminished after the growth of the first hBN monolayer. Indeed, our DFT calculations show that the adsorption of ammonia on hBN/Cu ( $-0.167$  eV, Figure 6a) and on hBN/hBN/.../Cu ( $-0.138$  eV, Figure 6b) is weaker than that of ammonia on bare Cu ( $-0.819$  eV); in fact, from a kinetics point of view, adsorption of ammonia is very inefficient at the growth temperature of  $900^\circ\text{C}$  ( $0.101$  eV). Using the Evans–Polanyi principle<sup>54</sup> that correlates activation barriers for dehydrogenation with the adsorption energies of surface intermediates (i.e.,  $\text{NH}_x$  radicals), we assess dehydrogenation trends via comparisons of the adsorption energies for  $\text{NH}_x$  on hBN/Cu ( $x = 1, 2$ ). The radicals  $\text{NH}_2$  and  $\text{NH}$  adsorb well on hBN/Cu (i.e., sufficiently large adsorption energies, Figure 6a), so we expect that the dehydrogenation is possible on hBN/Cu when ammonia stays adsorbed. This expectation is borne out in our experiments, which show that the growth of an hBN layer on top of hBN/Cu is not only possible, but also controllable via exposure times. Furthermore, because the exponential factors related to activation energies are the same orders of magnitude as those related to adsorption,<sup>55</sup> we can estimate how much slower the reaction proceeds on hBN/Cu in comparison to bare Cu(111) at the same temperature of  $900^\circ\text{C}$ . On the basis of adsorption energies of  $\text{NH}_2$ , the ratio of the corresponding activation rates is  $\exp[(-3.358 + 2.651)\text{eV}/k_{\text{B}}T] \approx 1/69$ , that is, the rate of growth on hBN/Cu is estimated to be about 69 times slower than that on Cu(111). This is consistent with our growth experiments in which we see a slow growth of the second hBN layer (Figure S3); the growth rate of the second layer is about 2 orders of magnitude slower than that of the first layer.

For growth of hBN layers atop the second one (Figure 6b), we report two important observations. First, ammonia adsorbs on hBN(0001) with an adsorption energy even weaker than that on hBN/Cu (Figure 6b). Second, the  $\text{NH}$  intermediate adsorbs with a significant energy on hBN(0001),  $-2.259$  eV; this strong adsorption is due to the  $\text{NH}$  radical in a bridge position wherein it bonds both with the N and the B atoms of the underlying BN sheet. While adsorption of ammonia and of  $\text{NH}$  on hBN(0001) are necessary conditions for enabling the growth of hBN layers past the second one, they are not

sufficient because the adsorption of  $\text{NH}_3$  and of  $\text{NH}_2$  on hBN(0001) are too weak. The adsorption of ammonia and its dehydrogenation to  $\text{NH}_2$  on the hBN/hBN/.../Cu(111) surface are therefore the bottlenecks impeding the formation of multilayer hBN on metal substrates that are rendered catalytically inactive by virtue of being covered with hBN. Thus far, we have not addressed the presence of radicals from the TEB on the surface. As illustrated by further DFT calculations and reactive molecular dynamics (MD) simulations, the presence of pyrolysis products from TEB (e.g., B and BH) on the surface is the key factor that enables multilayer hBN growth. Our DFT calculations show that B adatoms on hBN(0001) are strong binding sites for ammonia. The B adatoms attract  $\text{NH}_3$  in a facile manner when  $\text{NH}_3$  is placed within a lattice constant from them; furthermore, the adsorption energy at a B-adatom ( $-2.61$  eV) is significantly stronger than that on bare Cu ( $-0.819$  eV).

In order to gain further insights into the initial stages of new hBN layer formation on hBN(0001), we turn to reactive MD simulations on systems with N-based and B-based radicals on the surface (Methods). Because the time scales involved in this process are not accessible to DFT calculations, we use a realistic reactive force field (Reaxff)<sup>56</sup> to model the atomic interactions.<sup>57</sup> In our MD simulations, we employ equal number of  $\text{NH}_x$  radicals and B adatoms, amounting to one radical/adatom for every four surface unit cells; these simulations have been carried out at 900 and 1200 °C with similar results. In the beginning, the radicals diffuse on the surface and quickly form rather large clusters, some of which have a large number of “wrong” B–B or N–N bonds (Figure 7a). However, enabled by the presence of highly reactive B adatoms and sufficiently large temperatures, these clusters reorganize rapidly so as to increase the number of energetically favorable B–N bonds (refer to SI for thermodynamic arguments for B–N bond formation). The MD simulations show that this reorganization involves complex processes in which clusters diffuse, coalesce, and break apart; these processes result in the formation of BN polymers and six-atom rings. For example, Figure 7b shows that different polymerized B–N bonds/complexes coexist dynamically and diffuse on the surface; complexes with three (Figure 7b1), six (Figure 7b2), seven (Figure 7b3, ring with one B–N bond tethering), and 16 (Figure 7b4, ring with a 9-bond polymer tethering) contiguous B–N bonds can all be present simultaneously on the surface.

Our MD simulations give an estimate for the time scales required to form six-atom rings at the chosen surface coverage: 1 ring/ns at 900 °C, and 2 rings/ns, approximately, at 1200 °C. This information hopefully sets the stage for future comprehensive studies of hBN formation on passive substrates. Another important insight from MD simulations is an *a posteriori* confirmation that the temperature in our experiments is sufficient to drive the system toward forming six-atom rings by enabling it to cross barriers associated with highly complex processes (as opposed to the elementary process of dehydrogenation already discussed). The formation of these polymerized B–N bonds and six-atom rings is made possible strictly because of the pyrolysis products on the surface, because the catalytic action of the metal is completely obliterated by the previously deposited hBN layers. In this respect, the polymerization is not much different than that proposed to occur on metal surfaces, where diffusion and polymerization of BN bonds were enabled by the defects in the substrate.<sup>24</sup> A key difference in our work is that growth can

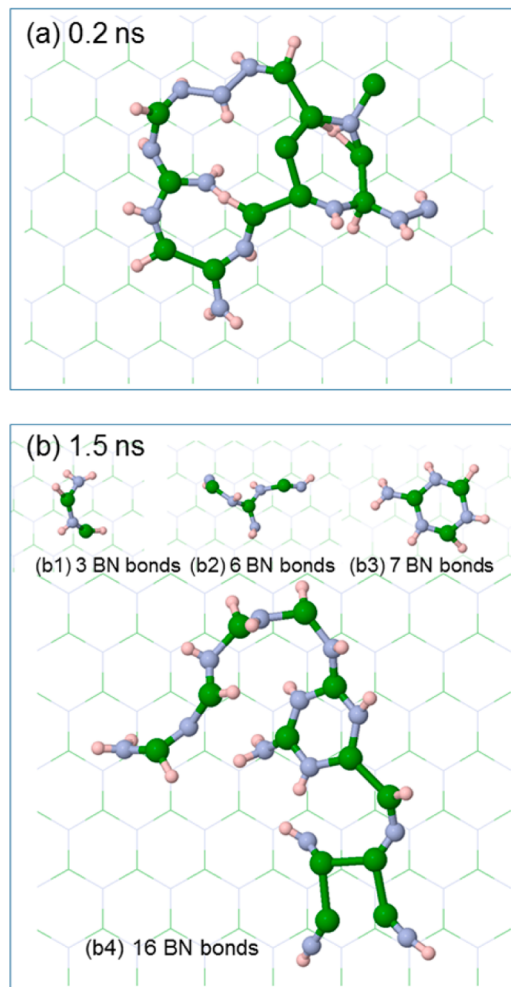


**Figure 7.** Six-atom ring formation in molecular dynamics simulations with the Reaxff potential. Atoms are colored green (B), light gray (N), white-pink (H). (a) Early on (0.2 ns), there are large clusters formed on the surface by virtue of diffusion of B-based and N-based radicals on the surface. (b1–b4) Clusters reorganize to six-atom rings with tethering polymerized B–N bonds (1.5 ns).

occur on perfect hBN substrates without any defects, because the pyrolysis products of the B-containing precursor enable, simultaneously, the dehydrogenation of ammonia and formation of complexes with BN bonds. These complexes ultimately polymerize, dehydrogenate, and form a new hBN layer.<sup>58</sup>

The above description of DFT calculations and MD simulations of ammonia and  $\text{NH}_x$  radicals on hBN(0001) in the presence of (some of the) TEB pyrolysis products brings evidence to support the mechanism proposed here. While simple, the mechanism is important in its versatility for a number of reasons. First, the idea of using radicals from one source to activate the other precursor is independent of the metallic substrate underneath. In fact, it could be operational for the growth of multilayers of hBN even on inert substrates such as sapphire,<sup>11,34</sup> because even though the hBN-covered substrate is not by itself active it becomes so because of the pyrolysis products that are adsorbed on it. Second, if the pyrolysis temperature for the B-containing precursor is attained at the surface, then the mechanism would be also independent of the precise nature of the B precursor. As such, it would be applicable to the growth from ammonia and diborane as well,

especially when all other plausible mechanisms have been ruled out.<sup>11</sup>

In conclusion, we have shown that a novel procedure for growing hBN layers on Cu(111) based on using independent precursors for B and N atoms goes beyond the usual limit of single monolayer, which is encountered when using a single, equiatomic precursor for B and N. We have proposed a mechanism that enables the multilayer growth to rely on the formation of active pyrolysis products of the TEB precursor, which strongly adsorb NH<sub>x</sub> radicals to facilitate the formation of BN bonds at the surface. Of key relevance for future applications is the excellent alignment of the hBN layers that emerges from this technique; the temperature is sufficiently high that hBN domains with high misorientation angles are unlikely, and in fact we never observe misorientations larger than 1.5°. A suite of characterization experiments allowed us to assess the quality and composition of the films. Unexpectedly, we have found that AFM in air allows us to observe the moiré superstructure of the first hBN layer and we have rationalized this observation in terms of the formation of a modulated interface dipole layer formed between hBN and Cu. These findings have improved our understanding of the mechanisms involved in growth of hBN and may help generate new growth methods for applications in which control over the number of layers and their alignment is crucial (such as tunneling barriers, ultrathin capacitors, and graphene-based devices).

**Methods. Growth and Characterization.** Copper films were deposited on sapphire substrates (c-plane) via sputtering at 100 °C. The substrates were then transferred to a low-pressure MOCVD reactor and annealed in hydrogen at 830 °C for 30 min. The substrates were then heated to 900 °C and the boron nitride films were grown at 20 Torr using precursors of triethylboron (TEB) and NH<sub>3</sub> for boron and nitrogen, respectively. The precursor V/III ratio was held at 1125 for growth of hBN films. The films were subsequently cooled to room temperature before being characterized.

The films were characterized using AFM, XRD, Raman, XPS, and TEM. The AFM was conducted with a Bruker Dimension Fast Scan using a standard TESPA tip in soft tapping mode to show surface topography and phase contrast. XRD  $\varphi$ - and  $2\theta$  scans were done using a PANalytical Empyrean X-ray diffractometer to measure crystallinity and alignment of the copper film on sapphire. Raman spectra were measured using a Renishaw inVia system that indicated the quality of the boron nitride films. XPS was also used to confirm the bonding nature of the boron nitride films and was collected using a PHI (PerkinElmer) 55000 XPS with an Al K<sub>a</sub> X-ray source. Cross-sectional TEM samples were prepared using the *in situ* FIB lift out technique on an FEI Dual Beam FIB/SEM. The samples were then imaged with a FEI Tecnai TF-20 FEG/TEM operated at 200 kV in high-resolution (HR) TEM mode.

**DFT Calculations.** We have used the plane-wave based package VASP<sup>59</sup> to perform DFT calculations in the framework of the generalized gradient approximation with the Perdew–Burke–Ernzerhof functional.<sup>60</sup> The interactions between hBN sheet(s) and a Cu(111) substrate are weak,<sup>18,61,62</sup> and we have modeled them in our calculations using the DFT-D2 method of Grimme.<sup>63</sup> There are two types of DFT results that we pursued: one is the calculation of adsorption energies on hBN/Cu and hBN(0001) and the other deals with calculating the variations of electronic density at the hBN–Cu and hBN–hBN/Cu interfaces in order to assess the origin of the AFM moiré patterns observed experimentally. For the calculation of

adsorption energies, our computational cells are lattice matched to hBN and consist of a three layer thick 4 × 4 Cu(111) slab with and without an hBN monolayer on it with an 18 Å vacuum spacing. The hBN sheet in our computational supercell has the registry with the Cu(111) substrate proposed by Bokdam et al. with the N atom atop a top layer Cu atom and the B atom above a hollow site.<sup>46</sup> Keeping fixed the bottom layer of Cu, the geometries were relaxed via conjugate-gradient in the presence of dipole corrections using a plane-wave cutoff of 500 eV, a Monkhorst–Pack  $k$ -point grid of 3 × 3 × 1, and a force tolerance criterion of 0.03 eV/Å. We have carried out spin-independent DFT calculations (geometry relaxations) calculations for ammonia and for the two reaction intermediates associated with the deposition of NH<sub>3</sub> on the surface, that is, NH and NH<sub>2</sub>. We have studied these intermediates on hBN/Cu(111) and hBN(0001), which are relevant for understanding the growth of the second and higher layers of hBN, respectively. The reactivity of surfaces is assessed through the adsorption of these reaction intermediates.

In order to understand the AFM response that we observed experimentally, we have performed calculations of interfacial electron transfer  $\Delta\rho$  at the hBN–Cu interface, and also at hBN–hBN/Cu interface (i.e., between the first two hBN layers). For the hBN–Cu interface, this is defined as the difference between the electron density of the hBN/Cu system and that of separate hBN and separate Cu at the same physical locations as they occupy in hBN/Cu,  $\Delta\rho_{\text{hBN/Cu}} = \rho_{\text{hBN/Cu}} - \rho_{\text{hBN}} - \rho_{\text{Cu}}$ . Similarly, for the hBN–hBN/Cu interface, the transfer is defined as  $\Delta\rho_{\text{hBN2/hBN1/Cu}} = \rho_{\text{hBN2/hBN1/Cu}} - \rho_{\text{hBN2}} - \rho_{\text{hBN1/Cu}}$ , where the labels 1 and 2 are given to the hBN layer in contact with the copper, and farther from it, respectively. These differences effectively describe the redistribution of charge due to the creation of the interface and represent the starting point for studying effects where interfacial charge dipoles are important.<sup>46,47,64–66</sup>

**Reaxff Molecular Dynamics Simulations.** All the molecular dynamics simulations were performed using the LAMMPS software,<sup>67</sup> while ReaxFF<sup>56</sup> has been employed to describe the interactions between B, N, and H atoms; the ReaxFF parameters were optimized against density functional theory calculations for ammonia borane.<sup>57</sup> The computational supercell consisted of 20 × 20 unit cells of hBN (0001); we placed adsorbed B adatoms or NH<sub>2</sub>/NH radicals on 25% of the surface unit cells chosen randomly. Note that B adatoms were placed only on N-sites, while the NH<sub>2</sub>/NH radicals were placed on the B-sites of the hBN surface (not on B-adatoms). Periodic boundary conditions were employed in the plane of the hBN(0001) surface, while a reflective wall was employed 10 Å above the hBN sheet. The system containing the hBN sheet and adatoms/radicals was first thermalized at 27 °C for 1 ns using canonical (NVT) MD simulations with a time step of 0.05 fs; constant temperature conditions were maintained using a Nose–Hoover thermostat. Thereafter, the temperature was ramped from 27 °C to the desired value over 0.1 ns and held at the final temperature (900 or 1200 °C) for 2 ns. During the MD simulations, the atoms belonging to the hBN surface were kept fixed, while the temporal evolutions of the B adatoms and NH<sub>2</sub>/NH radicals were monitored to identify the processes underlying formation of BN rings.

## ■ ASSOCIATED CONTENT

### Supporting Information

The Supporting Information is available free of charge on the ACS Publications website at DOI: [10.1021/acs.nanolett.6b05409](https://doi.org/10.1021/acs.nanolett.6b05409).

Additional details are available pertaining to growth procedure, AFM characterization showing the growth of the second hBN layer, Raman and AFM characterization of multilayer hBN films, and thermodynamic arguments in favor of six-atom ring formation ([PDF](#))

## ■ AUTHOR INFORMATION

### Corresponding Authors

\*E-mail: (C.V.C.) [cciobanu@mines.edu](mailto:cciobanu@mines.edu).

\*E-mail: (M.S.) [michael.snure.1@us.af.mil](mailto:michael.snure.1@us.af.mil).

### ORCID

Cristian V. Ciobanu: [0000-0002-8476-4467](https://orcid.org/0000-0002-8476-4467)

### Notes

The authors declare no competing financial interest.

## ■ ACKNOWLEDGMENTS

The authors gratefully acknowledge the support of the Air Force Office of Scientific Research under task number 16RYCOR331 and of the Sensors Directorate of the Air Force Research Laboratory. The authors would like to thank Timothy Prusnick and Gordon Grzybowski for their help with Raman and XPS characterization. HR-TEM work was performed by Evans Analytical Group. The authors gratefully acknowledge allocations for supercomputing resources from the high-performance computing centers of the Colorado School of Mines, Department of Defense, and Argonne National Laboratory.

## ■ REFERENCES

- (1) Dean, C. R.; Young, A. F.; Meric, I.; Lee, C.; Wang, L.; Sorgenfrei, S.; Watanabe, K.; Taniguchi, T.; Kim, P.; Shepard, K. L.; Hone, J. *Nat. Nanotechnol.* **2010**, *5*, 722–726.
- (2) Mayorov, A. S.; Gorbachev, R. V.; Morozov, S. V.; Britnell, L.; Jalil, R.; Ponomarenko, L. A.; Blake, P.; Novoselov, K. S.; Watanabe, K.; Taniguchi, T.; Geim, A. K. *Nano Lett.* **2011**, *11*, 2396–2399.
- (3) Britnell, L.; Gorbachev, R. V.; Jalil, R.; Belle, B. D.; Schedin, F.; Katsnelson, M. I.; Eaves, L.; Morozov, S. V.; Mayorov, A. S.; Peres, N. M. R.; Neto, A. H. C.; Leist, J.; Geim, A. K.; Ponomarenko, L. A.; Novoselov, K. S. *Nano Lett.* **2012**, *12*, 1707–1710.
- (4) Piquemal-Banci, M.; Galceran, R.; Caneva, S.; Martin, M. B.; Weatherup, R. S.; Kidambi, P. R.; Bouzehouane, K.; Xavier, S.; Anane, A.; Petroff, F.; Fert, A.; Robertson, J.; Hofmann, S.; Dubak, B.; Seneor, P. *Appl. Phys. Lett.* **2016**, *108*, 102404.
- (5) Shi, G.; Hanlumyuang, Y.; Liu, Z.; Gong, Y. J.; Gao, W. L.; Li, B.; Kono, J.; Lou, J.; Vajtai, R.; Sharma, P.; Ajayan, P. M. *Nano Lett.* **2014**, *14*, 1739–1744.
- (6) Kim, K. K.; Hsu, A.; Jia, X. T.; Kim, S. M.; Shi, Y. S.; Hofmann, M.; Nezich, D.; Rodriguez-Nieva, J. F.; Dresselhaus, M.; Palacios, T.; Kong, J. *Nano Lett.* **2012**, *12*, 161–166.
- (7) Caneva, S.; Weatherup, R. S.; Bayer, B. C.; Brennan, B.; Spencer, S. J.; Mingard, K.; Cabrero-Vilatela, A.; Baetz, C.; Pollard, A. J.; Hofmann, S. *Nano Lett.* **2015**, *15*, 1867–1875.
- (8) Song, L.; Ci, L. J.; Lu, H.; Sorokin, P. B.; Jin, C. H.; Ni, J.; Kvashnin, A. G.; Kvashnin, D. G.; Lou, J.; Yakobson, B. I.; Ajayan, P. M. *Nano Lett.* **2010**, *10*, 3209–3215.
- (9) Shi, Y. M.; Hamsen, C.; Jia, X. T.; Kim, K. K.; Reina, A.; Hofmann, M.; Hsu, A. L.; Zhang, K.; Li, H. N.; Juang, Z. Y.; Dresselhaus, M. S.; Li, L. J.; Kong, J. *Nano Lett.* **2010**, *10*, 4134–4139.
- (10) Oshima, C.; Nagashima, A. *J. Phys.: Condens. Matter* **1997**, *9*, 1–20.
- (11) Ismach, A.; Chou, H.; Ferrer, D. A.; Wu, Y. P.; McDonnell, S.; Floresca, H. C.; Covacevich, A.; Pope, C.; Piner, R.; Kim, M. J.; Wallace, R. M.; Colombo, L.; Ruoff, R. S. *ACS Nano* **2012**, *6*, 6378–6385.
- (12) Desrosiers, R. M.; Greve, D. W.; Gellman, A. J. *Surf. Sci.* **1997**, *382*, 35–48.
- (13) Corso, M.; Greber, T.; Osterwalder, J. *Surf. Sci.* **2005**, *577*, L78–L84.
- (14) Cavar, E.; Westerstrom, R.; Mikkelsen, A.; Lundgren, E.; Vinogradov, A. S.; Ng, M. L.; Preobrajenski, A. B.; Zakharov, A. A.; Martensson, N. *Surf. Sci.* **2008**, *602*, 1722–1726.
- (15) Muller, F.; Huefner, S.; Sachdev, H.; Laskowski, R.; Blaha, P.; Schwarz, K. *Phys. Rev. B: Condens. Matter Mater. Phys.* **2010**, *82*, 113406.
- (16) Sutter, P.; Lahiri, J.; Albrecht, P.; Sutter, E. *ACS Nano* **2011**, *5*, 7303–7309.
- (17) Park, J. H.; Park, J. C.; Yun, S. J.; Kim, H.; Luong, D. H.; Kim, S. M.; Choi, S. H.; Yang, W.; Kong, J.; Kim, K. K.; Lee, Y. H. *ACS Nano* **2014**, *8*, 8520–8528.
- (18) Joshi, S.; Ecija, D.; Koitz, R.; Iannuzzi, M.; Seitsonen, A. P.; Hutter, J.; Sachdev, H.; Vijayaraghavan, S.; Bischoff, F.; Seufert, K.; Barth, J. V.; Auwarter, W. *Nano Lett.* **2012**, *12*, 5821–5828.
- (19) Preobrajenski, A. B.; Vinogradov, A. S.; Ng, M. L.; Cavar, E.; Westerstrom, R.; Mikkelsen, A.; Lundgren, E.; Martensson, N. *Phys. Rev. B: Condens. Matter Mater. Phys.* **2007**, *75*, 245412.
- (20) Brugger, T.; Gunther, S.; Wang, B.; Dil, J. H.; Bocquet, M. L.; Osterwalder, J.; Winterlin, J.; Greber, T. *Phys. Rev. B: Condens. Matter Mater. Phys.* **2009**, *79*, 045407.
- (21) Lu, J.; Yeo, P. S. E.; Zheng, Y.; Xu, H.; Gan, C. K.; Sullivan, M. B.; Castro Neto, A. H.; Loh, K. P. *J. Am. Chem. Soc.* **2013**, *135*, 2368–2373.
- (22) Gao, Y.; Ren, W. C.; Ma, T.; Liu, Z. B.; Zhang, Y.; Liu, W. B.; Ma, L. P.; Ma, X. L.; Cheng, H. M. *ACS Nano* **2013**, *7*, 5199–5206.
- (23) Khan, M. H.; Huang, Z. G.; Xiao, F.; Casillas, G.; Chen, Z. X.; Molino, P. J.; Liu, H. K. *Sci. Rep.* **2015**, *5*, 09547.
- (24) Kim, S. M.; Hsu, A.; Park, M. H.; Chae, S. H.; Yun, S. J.; Lee, J. S.; Cho, D. H.; Fang, W. J.; Lee, C.; Palacios, T.; Dresselhaus, M.; Kim, K. K.; Lee, Y. H.; Kong, J. *Nat. Commun.* **2015**, *6*, 8662.
- (25) Xu, M. S.; Fujita, D.; Chen, H. Z.; Hanagata, N. *Nanoscale* **2011**, *3*, 2854–2858.
- (26) Reina, A.; Thiele, S.; Jia, X. T.; Bhaviripudi, S.; Dresselhaus, M. S.; Schaefer, J. A.; Kong, J. *Nano Res.* **2009**, *2*, 509–516.
- (27) Wang, M.; Kim, M.; Odkhoo, D.; Park, N.; Lee, J.; Jang, W. J.; Kahng, S. J.; Ruoff, R. S.; Song, Y. J.; Lee, S. *ACS Nano* **2014**, *8*, 5478–5483.
- (28) Reina, A.; Jia, X. T.; Ho, J.; Nezich, D.; Son, H. B.; Bulovic, V.; Dresselhaus, M. S.; Kong, J. *Nano Lett.* **2009**, *9*, 30–35.
- (29) Kwon, S. Y.; Ciobanu, C. V.; Petrova, V.; Shenoy, V. B.; Barenco, J.; Gambin, V.; Petrov, I.; Kodambaka, S. *Nano Lett.* **2009**, *9*, 3985–3990.
- (30) Mok, H. S.; Ebnonnasir, A.; Murata, Y.; Nie, S.; McCarty, K. F.; Ciobanu, C. V.; Kodambaka, S. *Appl. Phys. Lett.* **2014**, *104*, 101606.
- (31) Chubarov, M.; Pedersen, H.; Hogberg, H.; Czigany, Z.; Garbrecht, M.; Henry, A. *Chem. Mater.* **2015**, *27*, 1640–1645.
- (32) Kobayashi, Y.; Akasaka, T.; Makimoto, T. *J. Cryst. Growth* **2008**, *310*, 5048–5052.
- (33) Li, X.; Sundaram, S.; El Gmili, Y.; Ayari, T.; Puybaret, R.; Patriarche, G.; Voss, P. L.; Salvestrini, J. P.; Ougazzaden, A. *Cryst. Growth Des.* **2016**, *16*, 3409–3415.
- (34) Paduano, Q.; Snure, M.; Weyburne, D.; Kiefer, A.; Siegel, G.; Hu, J. J. *J. Cryst. Growth* **2016**, *449*, 148–155.
- (35) Fang, H. S.; Zhang, Z.; Pan, Y. Y.; Ma, R. H.; Liu, S.; Wang, M. Y. *Cryst. Res. Technol.* **2014**, *49*, 907–918.
- (36) Jang, A. R.; Hong, S.; Hyun, C.; Yoon, S. I.; Kim, G.; Jeong, H. Y.; Shin, T. J.; Park, S. O.; Wong, K.; Kwak, S. K.; Park, N.; Yu, K.; Choi, E.; Mishchenko, A.; Withers, F.; Novoselov, K. S.; Lim, H.; Shin, H. S. *Nano Lett.* **2016**, *16*, 3360–3366.

- (37) Holstein, W. L. *J. Electrochem. Soc.* **1988**, *135*, 1788–1793.  
(38) Koleske, D. D.; Wickenden, A. E.; Henry, R. L.; DeSisto, W. J.; Gorman, R. J. *J. Appl. Phys.* **1998**, *84*, 1998–2010.  
(39) Liu, S.; Stevenson, D. A. *J. Electrochem. Soc.* **1978**, *125*, 1161–1169.  
(40) Marom, N.; Bernstein, J.; Garel, J.; Tkatchenko, A.; Joselevich, E.; Kronik, L.; Hod, O. *Phys. Rev. Lett.* **2010**, *105*, 046801.  
(41) Constantinescu, G.; Kuc, A.; Heine, T. *Phys. Rev. Lett.* **2013**, *111*, 036104.  
(42) Gorbachev, R. V.; Riaz, I.; Nair, R. R.; Jalil, R.; Britnell, L.; Belle, B. D.; Hill, E. W.; Novoselov, K. S.; Watanabe, K.; Taniguchi, T.; Geim, A. K.; Blake, P. *Small* **2011**, *7*, 465–468.  
(43) Lu, G. Y.; Wu, T. R.; Yuan, Q. H.; Wang, H. S.; Wang, H. M.; Ding, F.; Xie, X. M.; Jiang, M. H. *Nat. Commun.* **2015**, *6*, 6160.  
(44) Kidambi, P. R.; Blume, R.; Kling, J.; Wagner, J. B.; Baehtz, C.; Weatherup, R. S.; Schloegl, R.; Bayer, B. C.; Hofmann, S. *Chem. Mater.* **2014**, *26*, 6380–6392.  
(45) Cho, Y. J.; Summerfield, A.; Davies, A.; Cheng, T. S.; Smith, E. F.; Mellor, C. J.; Khlobystov, A. N.; Foxon, C. T.; Eaves, L.; Beton, P. H.; Novikov, S. V. *Sci. Rep.* **2016**, *6*, 34474.  
(46) Bokdam, M.; Brocks, G.; Katsnelson, M. I.; Kelly, P. J. *Phys. Rev. B: Condens. Matter Mater. Phys.* **2014**, *90*, 085415.  
(47) Murata, Y.; Nie, S.; Ebnonnasir, A.; Starodub, E.; Kappes, B. B.; McCarty, K. F.; Ciobanu, C. V.; Kodambaka, S. *Phys. Rev. B: Condens. Matter Mater. Phys.* **2012**, *85*, 205443.  
(48) Jackson, J. D. *Classical Electrodynamics*, 3rd ed.; John Wiley & Sons, Inc., 1999; Chapter 4.  
(49) Liu, Y. Y.; Bhowmick, S.; Yakobson, B. I. *Nano Lett.* **2011**, *11*, 3113–3116.  
(50) Laskowski, R.; Blaha, P.; Schwarz, K. *Phys. Rev. B: Condens. Matter Mater. Phys.* **2008**, *78*, 045409.  
(51) Straumanis, M. E.; Yu, L. S. *Acta Crystallogr., Sect. A: Cryst. Phys., Diff., Theor. Gen. Crystallogr.* **1969**, *25*, 676–682.  
(52) Stehle, Y.; Meyer, H. M.; Unocic, R. R.; Kidder, M.; Polizos, G.; Datskos, P. G.; Jackson, R.; Smirnov, S. N.; Vlassiouk, I. V. *Chem. Mater.* **2015**, *27*, 8041–8047.  
(53) Jiang, Z.; Qin, P.; Fang, T. *Chem. Phys.* **2014**, *445*, 59–67.  
(54) Evans, M. G.; Polanyi, M. *Trans. Faraday Soc.* **1936**, *32*, 1333–1360.  
(55) Pallassana, V.; Neurock, M. *J. Catal.* **2000**, *191*, 301–317.  
(56) Chenoweth, K.; van Duin, A. C. T.; Goddard, W. A. *J. Phys. Chem. A* **2008**, *112*, 1040–1053.  
(57) Weismiller, M. R.; van Duin, A. C. T.; Lee, J.; Yetter, R. A. *J. Phys. Chem. A* **2010**, *114*, 5485–5492.  
(58) Park, S.; Lee, J.; Kim, H. S.; Park, J. B.; Lee, K. H.; Han, S. A.; Hwang, S.; Kim, S. W.; Shin, H. J. *ACS Nano* **2015**, *9*, 633–638.  
(59) Kresse, G.; Furthmüller, J. *Phys. Rev. B: Condens. Matter Mater. Phys.* **1996**, *54*, 11169–11186.  
(60) Perdew, J. P.; Burke, K.; Ernzerhof, M. *Phys. Rev. Lett.* **1996**, *77*, 3865–3868.  
(61) Koitz, R.; Seitsonen, A. P.; Iannuzzi, M.; Hutter, J. *Nanoscale* **2013**, *5*, 5589–5595.  
(62) Preobrajenski, A. B.; Vinogradov, A. S.; Martensson, N. *Surf. Sci.* **2005**, *582*, 21–30.  
(63) Grimme, S. *J. Comput. Chem.* **2006**, *27*, 1787–1799.  
(64) Murata, Y.; Starodub, E.; Kappes, B. B.; Ciobanu, C. V.; Bartelt, N. C.; McCarty, K. F.; Kodambaka, S. *Appl. Phys. Lett.* **2010**, *97*, 143114.  
(65) Kappes, B. B.; Ebnonnasir, A.; Kodambaka, S.; Ciobanu, C. V. *Appl. Phys. Lett.* **2013**, *102*, 051606.  
(66) Ebnonnasir, A.; Narayanan, B.; Kodambaka, S.; Ciobanu, C. V. *Appl. Phys. Lett.* **2014**, *105*, 031603.  
(67) Plimpton, S. *J. Comput. Phys.* **1995**, *117*, 1–19.